

# Exploring the Zero-Shot Capabilities of the Segment Anything Model (SAM) in 2D Medical Imaging: A Comprehensive Evaluation and Practical Guideline

Christian Mattjie<sup>1</sup>, Luis Vinicius de Moura<sup>1</sup>, Rafaela Cappelari Ravazio<sup>1</sup>,  
Lucas Silveira Kupssinski<sup>1</sup>, Otávio Parraga<sup>1</sup>, Marcelo Mussi Delucis<sup>1</sup>, and  
Rodrigo Coelho Barros<sup>1</sup>

School of Technology, Pontifícia Universidade Católica do Rio Grande do Sul  
Av. Ipiranga, 6681, 90619-900, Porto Alegre, RS, Brazil  
`christian.oliveira95@edu.pucrs.br`  
`rodrigo.barros@pucrs.br`

**Abstract.** Segmentation in medical imaging plays a crucial role in diagnosing, monitoring, and treating various diseases and conditions. The current landscape of segmentation in the medical domain is dominated by numerous specialized deep learning models fine-tuned for each segmentation task and image modality. Recently, the Segment Anything Model (SAM), a new segmentation model, was introduced. SAM utilizes the ViT neural architecture and leverages a vast training dataset to segment almost any object. However, its generalizability to the medical domain remains unexplored. In this study, we assess the zero-shot capabilities of SAM 2D in medical imaging using eight different prompt strategies across six datasets from four imaging modalities: X-ray, ultrasound, dermatoscopy, and colonoscopy. Our results demonstrate that SAM's zero-shot performance is comparable and, in certain cases, superior to the current state-of-the-art. Based on our findings, we propose a practical guideline that requires minimal interaction and yields robust results in all evaluated contexts.

**Keywords:** Medical Imaging · Segmentation · Segment Anything Model · Zero-shot · Deep Learning.

## 1 Introduction

Medical imaging plays an essential role in diagnosing, monitoring, and treating various diseases and conditions [1]. In many cases, accurate segmentation of these images is crucial to extract useful information and help perform clinical decision-making. However, segmentation methods rely heavily on time-consuming, manually engineered features and error-prone thresholding designed for specific scenarios with poor generalization to new images [2]. Outstanding progress has been achieved in medical image segmentation since the introduction of deep learning

(DL) techniques due to their capacity to learn intrinsic features and patterns from big datasets [3, 4, 5].

However, medical image segmentation is especially challenging for DL because there is a considerable cost associated with specialized professionals labeling images, and as a consequence, data is scarce. There is also not much evidence on the capacity of DL models trained on natural images to extrapolate to medical application settings.

The DL revolution began with the breakthrough of Convolutional Neural Networks (CNNs) in computer vision applications [6]. However, there is now a new wave of innovative applications based on the Transformer architecture [7]. Transformers leverage the training process to take advantage of larger datasets and create models capable of generalizing to unseen distributions and even to different tasks.

Recently, Segment Anything Model (SAM) [8], a state-of-the-art vision transformer (ViT) capable of generating segmentation masks for virtually anything, has been made publicly available. SAM also introduced the notion of prompting in the context of image segmentation, to prompt the segmentation model is to guide its inference process by providing points inside the region of interest (ROI) or by drawing a bounding box around it.

In this paper, we evaluate the zero-shot capabilities of SAM in segmenting 2D medical images. We assess its performance in six datasets from four different imaging modalities: X-ray, ultrasound, dermatoscopy, and colonoscopy. We investigate different prompting strategies in order to provide a guideline on the most effective ways one can use SAM in the medical image domain. These medical imaging modalities are widely used in various medical fields, and accurate segmentation may assist in the diagnosis and treatment of several diseases.

## 2 Related Work

### 2.1 Medical Image Segmentation

Medical image segmentation is an essential component of medical imaging analysis that focuses on identifying and delineating structures or regions, such as organs, tissues, or lesions. Accurate segmentation is essential for various clinical applications, including diagnosis, treatment, and monitoring of disease progression. It enables critical tasks such as measuring tissue volume for tracking growth and delineating radiosensitive organs for radiotherapy treatment.

In the current landscape of medical image segmentation, there are specific methods particular to the application, imaging modality, and body part studied [9, 10]. However, automatic segmentation remains a challenging task due to the complexity of medical images and data scarcity. The output of the segmentation algorithm is also affected by several factors, including the partial volume effect, intensity inhomogeneity, presence of artifacts, and the lack of contrast between the soft regions [11].

DL techniques have gained significant traction in medical image segmentation due to their capacity for capturing complex patterns and representations

from large-scale datasets. Among the most widely used DL approaches for medical image segmentation are CNNs. Largely used models for medical image segmentation include U-Net [3] and its variants, which are designed explicitly for biomedical image segmentation. U-Net employs a symmetric encoder-decoder architecture that enables the model to capture both high-level contextual information and fine-grained details, leading to improved segmentation outcomes.

Recently, new state-of-the-art segmentation techniques have been introduced in the field, such as the training of DL models in polar images [12], incorporating textual information with vision-language models [4], and using attention mechanisms with CNNs in ViTs [13].

## 2.2 Vision Transformer (ViT)

ViTs are a class of DL models that employ transformer architecture [14]. These models process images by dividing them into fixed-size, non-overlapping patches and then linearly embedding these patches into a flat sequence of tokens. Each token is then passed through a series of self-attention layers to learn relevant contextual relationships and spatial information, enabling the model to discover semantically rich patterns [7].

ViTs are resilient to some of the inductive biases present in CNNs, such as locality and translation equivariance. A lower inductive bias allows ViTs to be more flexible but requires more data to generalize. The data demand could restrict the use of ViTs in medical imaging, where data is scarce. However, by capitalizing on pre-training and fine-tuning, the ViTs are overtaking computer vision with impressive generalization performance [15, 16].

Recently, ViTs achieved outstanding results in zero-shot learning [17, 18, 19]. Such a setting is challenging since the model must learn to generalize for even classes and contexts not seen during training. That is also the case for medical imaging, where ViT-based models achieve the most state-of-the-art results [20, 21, 13].

## 3 Method

### 3.1 Segment Anything Model (SAM)

SAM [8] is a state-of-the-art ViT trained on the SA-1B dataset, which contains 11 million images and 1 billion masks, making it the largest image segmentation dataset available today. SAM’s accuracy has been demonstrated in its ability to segment various objects and shapes, proving its capacity to segment anything in a 2D image effectively. SAM operates by either segmenting all objects present in an input image or by leveraging prompts that explicitly indicate the target region for segmentation. These prompts may be points identifying the region of interest or regions that should not be included. It is also possible to input a bounding box delimiting the area where the object of interest is. Initial results with the SAM model suggest outstanding quality in the segmentation masks

and zero-shot generalization to new scenes and unseen objects. Yet, there are virtually no medical images in SAM’s training data. So it is still an open question if it is able to generalize to this domain.

To avoid problems due to ambiguous prompts, SAM generates a set of three masks and scores corresponding to different interpretations of the intended region. The first mask in the output sequence is the smallest, capturing the most conservative interpretation of the intended region based on the given prompt. As the sequence progresses, the subsequent masks expand in size, with each mask incorporating the previous one. The score returned for each mask is a value indicating the confidence of SAM in the designated prediction. This design enables SAM to cover a broader range of possible segmentation outcomes, reflecting the model’s attempt to account for the ambiguity in the size of the target region due to the prompt’s limited information.

In practical applications, particularly within the domain of medical imaging, it is crucial to ensure that the model accurately identifies and segments the relevant structures or regions of interest. Due to this requirement, our study opted to focus on input prompt strategies for guiding SAM’s segmentation process. The rationale for this choice lies in the inherent uncertainties associated with the segment-everything approach, where the model’s understanding of the segmented objects cannot be guaranteed. Consequently, by utilizing prompts, we aimed to enhance SAM’s segmentation capabilities in medical imaging tasks and provide a more reliable and controlled evaluation of its performance. Additionally, we did not consider the confidence scores provided by SAM for each mask, as these scores reflect the quality of the segmentation without accounting for the accuracy of the target region in relation to the intended object.

SAM’s ViT architecture has three different iterations, each with distinct trade-offs regarding processing needs and model performance: ViT Base (ViT-B), ViT Large (ViT-L), and ViT Huge (ViT-H). The main distinction between these variations is the model’s number of layers and parameters, shown in Table 1. As the number of layers and parameters grows, the model gets more powerful and is able to capture more complex aspects of the input images. However, larger models need more computing power, which can be a drawback in some settings. Still, even the largest iteration of SAM is fairly small.

Architecture	Transformer Layers	Parameters	Size (Mb)
ViT-B	12	91M	776
ViT-L	24	308M	1582
ViT-H	32	636M	2950

**Table 1.** Summary of SAM’s ViT architecture variations.



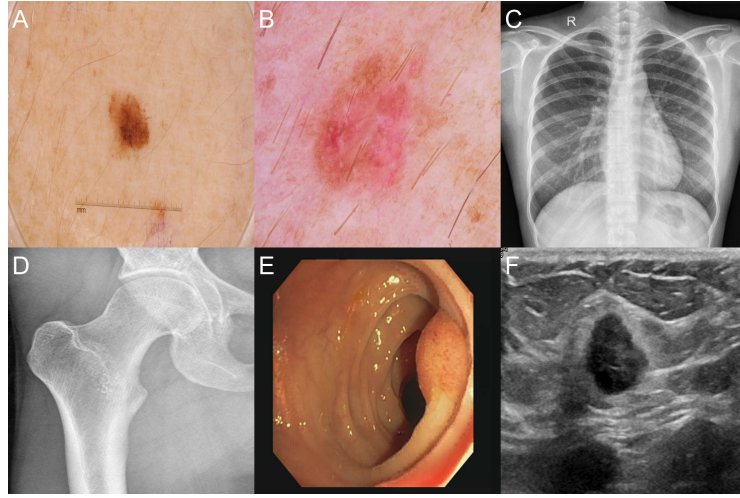


**Fig. 1.** Samples from each of the six datasets used in this study. A: ISIC, B: HAM, C: CXR, D: HJXR, E: CVC, F: BUSI.

### 3.2 Datasets

For our evaluation of the SAM, we used six datasets from four medical imaging modalities: X-ray, Ultrasound, dermatoscopic, and colonoscopy images. Our primary objective was to assess the model’s performance and versatility when prompted with various strategies, simulating a physician’s approach to segmenting specific organs or ROIs in medical images. Figure 1 shows a sample from each dataset.

- ISIC 2018 [22] (ISIC) is a publicly available dataset of skin lesion images containing 2594 dermatoscopic images of skin lesions of different types, sizes, and colors from 2056 unique patients with accompanying segmentation masks. The resolution of the images varies from 640x480 to approximately 6700x4400 pixels, which are provided in JPEG format. The masks have the same resolution as the corresponding image. They are generated by expert dermatologists using a manual annotation tool, and a second expert has reviewed each one to ensure accuracy.
- HAM10000 [23] (HAM) is a publicly available dataset of skin lesion images containing 10015 dermatoscopic images of skin lesions of different types, sizes, and colors from 7388 unique patients. The resolution of all images is 640x450, and they are provided in JPEG format. Recently, Tschandl, P. et al. [24] provided expert segmentation masks for all images with the corresponding resolution.
- Montgomery-Shenzhen [25, 26] (CXR) is a fusion of two publicly available chest X-ray datasets. The name comes from the respective hospitals where the data was collected. It comprises 800 X-ray images, with 704 accom-

panying lung segmentation masks manually created by expert radiologists dataset, available in PNG format.

- X-ray images of the hip joints [27] (HJXR-F, HJXR-I) is a publicly available dataset of X-ray images of the lower legs. It comprises 140 images with an average resolution of  $327 \times 512$  and corresponding segmentation masks for the femur and ilium separately. The images and masks are available in NII format.
- CVC-ClinicDB [28] (CVC) is a publicly available dataset of 612 images from 31 colonoscopy sequences. The resolution of the images is  $384 \times 288$ , and they are provided in PNG format. Segmentation masks for the polyps, created by expert gastroenterologists, are also provided for all available images.
- Breast Ultrasound Images [29] (BUSI) is a publicly available dataset of ultrasound images of the breast. It comprises 780 images from 600 patients with an average size of  $500 \times 500$  pixels, provided in PNG format. The images are categorized into normal, benign, and malignant. Segmentation masks for the tumors are provided for benign and malignant cases.

### 3.3 Prompt Strategies

A physician could be instructed to guide the segmentation procedure in many ways (e.g., clicking in the region of interest, clicking outside the region of interest, or drawing a bounding box). To simulate plausible prompting strategies, we performed several experiments:

- Using only the central point of the ground-truth mask, which is expected to be the most informative single-point prompt;
- We eroded the ground-truth mask and then selected a random point within it, representing minimal guidance;
- We eroded the ground-truth mask and then divided it vertically into sections, selecting a random point within each one to provide a more distributed set of prompts;
- Prompting with the bounding box of the ground-truth mask, providing a more explicit spatial constraint for segmentation; and
- Modifying the bounding box in size and position by a portion of the ground-truth mask size, simulating variations in the accuracy of a physician’s initial assessment.

For the multiple points strategy, we divided the mask into three and five sections, and for the varied bounding box strategy, we randomly altered its size and position up to 5%, 10%, and 20% of the ground-truth mask. Given these variations, we ran a total of eight experiments per model/dataset, which are shown in Figure 2: central-point (CP), random-point (RP), random-points-3 (RP3), random-points-5 (RP5), bounding-box (BB), bounding-box-similar-5 (BBS5), bounding-box-similar-10 (BBS10) and bounding-box-similar-20 (BBS20).

In RP, RP3, and RP5 methods, we apply the erosion morphological operator to the ground truth mask before selecting a random point inside the resulting

region. This procedure ensures the selected point is not near the edges of the region of interest while also maintaining the randomness in the prompting procedure, which is expected in real-world scenarios. The value of the erosion was determined according to the dataset: On CXR and ISIC datasets, where the regions are larger, we used 30 pixels; for the CVC dataset, which contains tiny images that would be eroded entirely, we used a value of 1 pixel; for all the other datasets, which also contains small regions we used a value of 10 pixels.

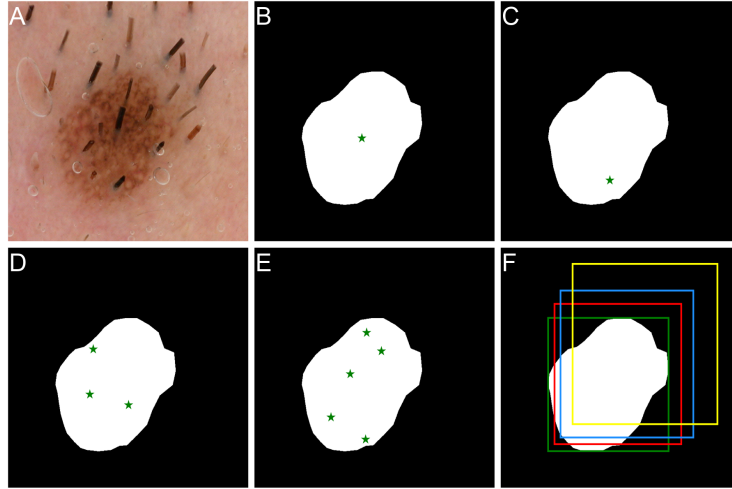


**Fig. 2.** Example of all prompt strategies on a skin lesion image and mask. A: original image, B: CP, C: RP, D: RP3, E: RP5, F: BB in green, BBS5 in red, BBS10 in blue, and BBS20 in yellow. The size and position shown are their max variation for BBS methods, while in our experiments, they were altered randomly.

### 3.4 Preprocessing

During our experiments, we addressed several challenges that arose due to the nature of the datasets. For instance, we employed a fill-holes technique to correct mask information, particularly in the ISIC dataset, where some masks only contoured the relevant lesion. Additionally, in cases where multiple masks were present per image (e.g., two lungs or two skin lesions), we identified the two largest regions and processed them individually (using the prompt strategies from Section 3.3) to ensure accurate and precise segmentation. We manually inspected all images to verify that there weren't any with three relevant and separate regions. Once the model generated predictions for both regions, we merged them into a single prediction.

On the HJXR dataset, the only one with images in a format incompatible with SAM, we converted them from NII to PNG, normalizing the values between

0 and 255. Since masks were available for the femur and ilios individually for every image in the dataset, we evaluated the predictions separately (HJXR-F and HJXR-I, respectively).

### 3.5 Evaluation

The Dice Similarity Coefficient (DSC) is a widely used statistical metric for measuring the accuracy of image segmentation. It quantifies the similarity between two sets of data, typically represented as binary arrays, by comparing a predicted segmentation mask with the ground-truth one. The DSC ranges from one to zero, with one indicating a perfect match and zero signifying a complete mismatch. This metric facilitates the assessment of the performance difference between classifiers, making it a valuable tool for evaluating segmentation algorithms. It can be computed as follows:

$$DSC = \frac{2|Y \cap Y'|}{|Y| + |Y'|} \quad (1)$$

Where  $Y$  and  $Y'$  refer to the ground-truth and predicted segmentation mask, respectively.

## 4 Results and Discussion

In this section, we present the results of the experiments performed contemplating six datasets, eight prompting strategies, and three variations of the SAM model. We compare these results to current SOTA methods, with some zero-shot results of SAM surpassing the benchmarks. We follow by qualitatively discussing the results and presenting some challenging hand-picked images to illustrate our points. We close the section with a guideline for physicians to use SAM that is practical to implement, requires minimal interaction, and produces solid results.

Table 2 shows the DSC of the predictions for ViT-H, the largest model of SAM, over six datasets using the eight proposed prompt strategies. Results for all models are shown in the Supplementary Material Table 5. 1st, 2nd, and 3rd refer to the three predictions generated by SAM. Figure 3 shows an example of these predictions in the CXR dataset for RP5 and BBS10 strategies. We can see that the RP5 method has a higher distinction of predictions, whereas the BBS10 method is more consistent. This may be the case because the bounding box indicates both the region to be segmented and the regions that shouldn't be (outside the box).

In a practical scenario, a physician may choose which of the three predictions best fits the corresponding region. To emulate this process, we evaluated the highest DSC per image, regardless of its position among the three predictions. We present those results in Table 3. This approach yielded a modest improvement of approximately 1% compared to automatically selecting a prediction (Table 2). Although the overall gain is small, it is significant for certain subjects and requires minimal effort from the physician.

Dataset	Pred	CP	RP	RP3	RP5	BB	BBS5	BBS10	BBS20
ISIC	1st	0.538	0.531	0.762	0.774	0.745	0.737	0.715	0.603
	2nd	0.718	0.677	0.769	0.788	0.845	0.842	0.833	0.789
	3rd	0.375	0.363	0.390	0.483	<b>0.872</b>	0.868	0.860	0.816
HAM	1st	0.544	0.527	0.752	0.765	0.732	0.724	0.700	0.589
	2nd	0.729	0.686	0.768	0.785	0.838	0.835	0.824	0.778
	3rd	0.420	0.406	0.443	0.541	<b>0.865</b>	0.861	0.851	0.809
CXR	1st	0.904	0.863	0.923	0.927	0.936	0.934	0.911	0.686
	2nd	0.758	0.727	0.766	0.828	<b>0.942</b>	0.939	0.929	0.826
	3rd	0.471	0.469	0.482	0.514	0.935	0.930	0.913	0.803
HJXR-F	1st	0.876	0.822	0.941	0.948	0.924	0.908	0.848	0.618
	2nd	0.743	0.767	0.767	0.776	<b>0.962</b>	0.958	0.904	0.746
	3rd	0.517	0.543	0.548	0.599	0.949	0.945	0.905	0.723
HJXR-I	1st	0.211	0.742	0.808	0.828	<b>0.875</b>	0.866	0.734	0.624
	2nd	0.393	0.479	0.449	0.491	0.855	0.849	0.790	0.620
	3rd	0.294	0.295	0.316	0.384	0.800	0.796	0.758	0.629
CVC	1st	0.716	0.763	0.861	0.880	0.889	0.881	0.835	0.702
	2nd	0.554	0.544	0.642	0.754	<b>0.926</b>	0.924	0.916	0.844
	3rd	0.232	0.224	0.224	0.245	0.924	0.922	0.918	0.868
BUSI	1st	0.583	0.541	0.736	0.766	0.754	0.744	0.713	0.631
	2nd	0.641	0.616	0.688	0.735	0.840	0.837	0.823	0.768
	3rd	0.192	0.184	0.196	0.254	<b>0.863</b>	0.859	0.848	0.800

**Table 2.** DSC of predictions for the ViT-H model for six datasets using the eight proposed prompt strategies considering the 1st, 2nd, and 3rd prediction.

Dataset	Model	CP	RP	RP3	RP5	BB	BBS5	BBS10	BBS20
ISIC	ViT-H	0.788	0.768	0.820	0.835	<u>0.877</u>	0.874	0.866	0.829
	ViT-L	0.783	0.768	0.811	0.818	<u>0.876</u>	0.872	0.864	0.819
	ViT-B	0.764	0.733	0.804	0.815	<b>0.879</b>	0.876	0.864	0.822
HAM	ViT-H	0.782	0.764	0.812	0.824	<u>0.870</u>	0.866	0.857	0.820
	ViT-L	0.784	0.772	0.809	0.819	<u>0.867</u>	0.864	0.854	0.809
	ViT-B	0.745	0.706	0.785	0.796	<b>0.872</b>	0.867	0.855	0.810
CXR	ViT-H	0.922	0.902	0.928	0.936	<u>0.952</u>	0.950	0.942	0.862
	ViT-L	0.929	0.917	0.932	0.930	<b>0.954</b>	0.952	0.943	0.849
	ViT-B	0.915	0.893	0.930	0.935	<u>0.948</u>	0.943	0.932	0.858
HJXR-F	ViT-H	0.906	0.917	0.943	0.950	<b>0.973</b>	<b>0.973</b>	0.957	0.861
	ViT-L	0.910	0.916	0.939	0.948	<b>0.973</b>	<b>0.973</b>	0.956	0.880
	ViT-B	0.927	0.882	0.910	0.907	<u>0.971</u>	0.969	0.950	0.870
HJXR-I	ViT-H	0.483	0.786	0.808	0.828	<u>0.889</u>	0.886	0.843	0.719
	ViT-L	0.478	0.841	0.865	0.860	<b>0.894</b>	0.889	0.839	0.726
	ViT-B	0.500	0.765	0.825	0.830	<u>0.875</u>	0.870	0.838	0.696
CVC	ViT-H	0.838	0.854	0.884	0.898	<b>0.940</b>	0.938	0.934	0.889
	ViT-L	0.815	0.823	0.848	0.847	<u>0.934</u>	0.931	0.920	0.869
	ViT-B	0.739	0.749	0.783	0.784	<u>0.932</u>	0.930	0.921	0.851
BUSI	ViT-H	0.732	0.706	0.791	0.816	<u>0.870</u>	0.868	0.855	0.813
	ViT-L	0.744	0.727	0.800	0.807	<u>0.875</u>	0.872	0.865	0.810
	ViT-B	0.734	0.701	0.804	0.818	<b>0.886</b>	0.884	0.874	0.831

**Table 3.** DSC of predictions for all variations of SAM for six datasets using the eight proposed prompt strategies. For each set of predictions, only the one with the highest DSC was considered.

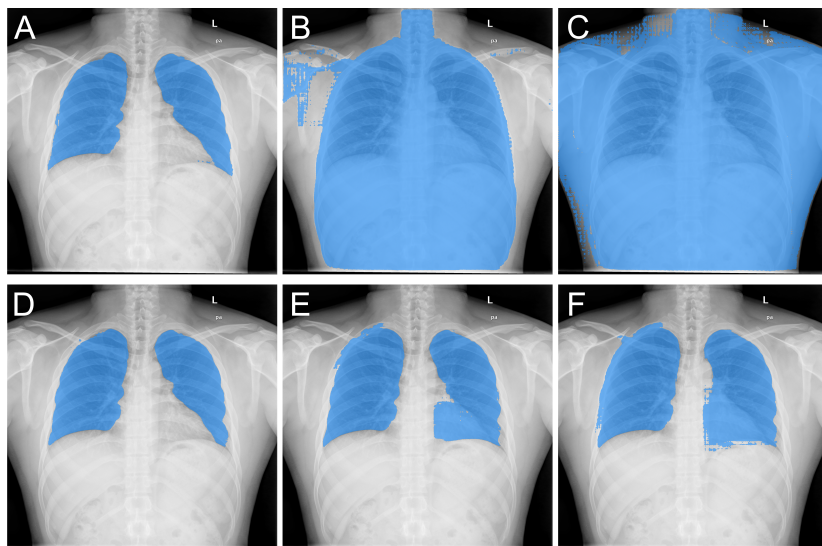


**Fig. 3.** Three returning predictions from SAM using RP5 (A, B, C) and BBS10 (D, E, F) input methods for the CXR dataset. A physician may choose the one that best suits the corresponding region to be segmented.

The bounding box (BB) strategy consistently demonstrated the highest performance across all datasets, as evidenced in Tables 2 and 3. Even with a variation of 5 or 10% (BBS5, BBS10), this method outperformed all point prompt strategies, while BBS20 achieved comparable results to RP5. This indicates the reliability of the bounding box method, even with minor errors when delineating the target segmentation region.

As for point prompt methods (CP, RP, RP3, RP5), increasing the number of input points resulted in better model performance. However, these methods could not surpass the BB, BBS5, and BBS10 strategies. Additionally, RP5 demands greater manual intervention, making it more labor-intensive compared to using a bounding box.

It is worth noting that our experiments do not account for additional prompt points that can be added post-prediction to refine the segmentation. This refinement process can be applied to both include regions omitted from the prediction and remove regions that should not be part of the segmentation. Consequently, physicians can achieve even more accurate segmentations with minimal additional effort.

Remarkably, the ViT-B model achieved similar performance to the larger variations of SAM, in some cases even surpassing them. Furthermore, due to its modest GPU memory requirements, it can be easily used with affordable hardware, making SAM’s application in medical imaging highly accessible without substantial investment.

#### 4.1 Comparison with state-of-the-art (SOTA) segmentation models

We use the intermediate size SAM (ViT-L) for comparison with other SOTA models. Table 4 compares the performance of SAM using the BB5 strategy (simulating a physician annotating with a small error, then choosing the best of the three segmentations) with state-of-the-art (SOTA) models employed in each dataset. We did not find other models evaluated in the HJXR dataset for comparison.

Dataset	Model	DSC
ISIC	Rema-net [5]	0.944
	SAM	0.872
HAM	Rema-net [5]	0.936
	SAM	0.864
CXR	Attention U-Net [30]	0.982
	ReSE-Net[31]	0.976
	SAM	0.952
CVC	FSA-Net [32]	0.947
	SAM	0.931
BUSI	PODDA,A. et al [33]	0.826
	SAM	0.872
HJXR-F	SAM	0.973
HJXR-I	SAM	0.889

**Table 4.** Comparison of the results of the BBS5 strategy using the ViT-L model with the current state-of-the-art DL models.

SAM achieved extraordinary results for a zero-shot approach compared with the SOTA. In the BUSI dataset, SAM outperformed the SOTA by approximately 5%, maintaining its leading performance even with the BBS20 strategy, which allows for a large margin of error in the annotation process. In the CVC dataset, SAM’s performance trailed by less than 2%, while in the CXR dataset, the gap was 3%.

Despite the absence of comparable studies, SAM demonstrated an impressive 0.973 DSC for femur segmentation. The ilios segmentation, a more challenging task due to lower contrast with the surrounding regions, stems from the attenuation caused by the X-ray. In the leg, however, the femur is the only structure with such a distinct attenuation. Given these factors, the results for ilios segmentation were also praiseworthy, with a 0.889 DSC.

For the ISIC and HAM datasets, SAM’s performance was around 7% lower. However, it is essential to consider the unique characteristics of these datasets, as discussed in Section 4.2. Furthermore, the large volume of available data (over 10,000 images) makes training task-specific DL models more feasible for these tasks. Conversely, with small datasets like BUSI, training an end-to-end DL model is challenging due to limited data availability. In such situations, using a



model like SAM is more practical, as it benefits from exposure to extensive data across various domains.

## 4.2 Qualitative Analysis

Handling medical images is inherently challenging due to the unique characteristics of each dataset. In the case of the CXR dataset, which comprises chest X-rays and their corresponding segmentations, we encountered inconsistencies in the segmented regions, as illustrated in Figure 4. Some ground-truth masks included the heart, while others omitted it. However, SAM can quickly rectify these segmentation deviations by having the user choose the prediction that best suits it, as shown in Figure 3, or by adding input points to include or exclude areas as necessary.

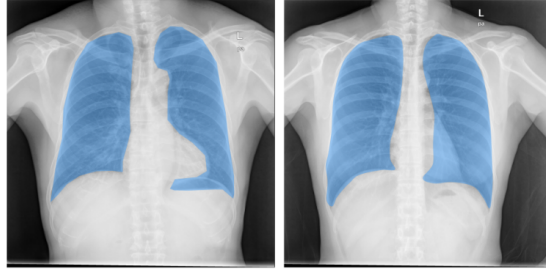


**Fig. 4.** Example of inconsistencies in the ground-truth region in the CXR dataset.

The conventional DICOM format for X-ray images typically features a 12 or 16-bit depth, allowing physicians to adjust the window/level for better tissue and organ visualization. We hypothesize that refining the window/level during conversion to JPEG or PNG could enhance tissue delimitation and potentially improve SAM’s performance for this imaging modality. However, we did not evaluate this approach, as the CXR dataset is provided in PNG format, and the HJXR dataset was normalized and converted to PNG using its maximum and minimum values.

For the ISIC dataset, which consists of skin lesion images, we observed numerous poorly annotated ground-truth masks, as evidenced in Figure 5. This inaccuracy influenced our DSC results, as the masks generated by SAM appear to be more precise than the original masks. Furthermore, the presence of body hair in the ISIC and HAM datasets significantly impacts the segmentation process, particularly when utilizing point prompt strategies. A hair crossing a lesion may incorrectly suggest two separate regions rather than one. To circumvent this issue, bounding box strategies can be employed to provide adequate information to the model. Nevertheless, SAM excludes the hair from the segmentation, which worsens its performance. The skin lesion datasets have yet another obstacle due

to imprecise lesion edges, making accurate segmentation of skin lesions a challenging task.

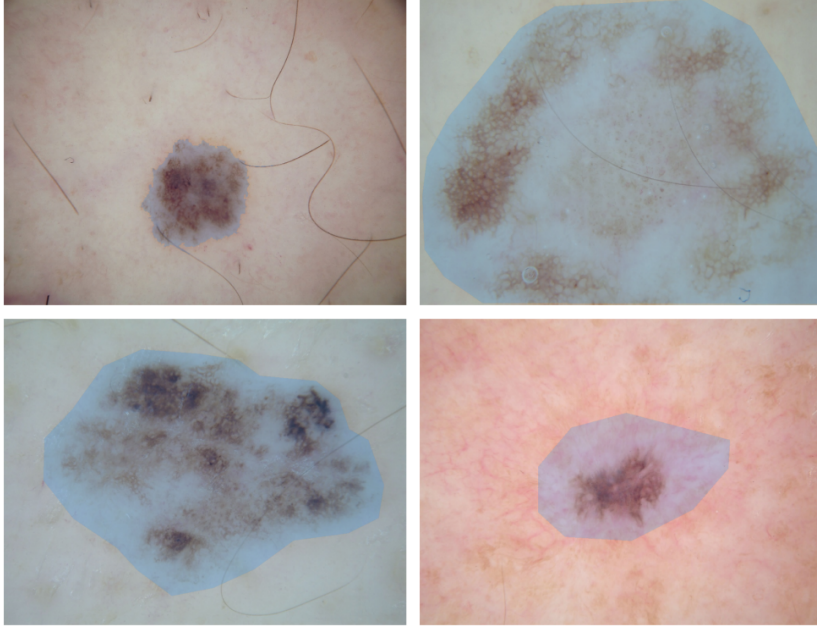


**Fig. 5.** Example of inconsistencies in the ground-truth region in the ISIC dataset.

Ultrasound images pose significant challenges for DL models due to their inhomogeneous intensities and low signal-to-noise ratio, which complicates outlining breast tumors in datasets such as BUSI. Moreover, the absorption and reflection of ultrasound can generate artifacts in the image, further complicating the segmentation task, even in fine-tuned models. Nevertheless, SAM achieved remarkable results in this dataset but also encountered difficulties in accurately segmenting the boundaries of breast tumors due to the blurred edges inherent in ultrasound images.

### 4.3 Guideline

Based on our findings, we present a practical guideline for employing the Segment Anything Model (SAM) in medical imaging tasks. By following this approach, physicians can harness the potential of SAM to achieve accurate segmentation results while maintaining control over the process. We advise using the largest SAM model compatible with the available hardware; however, any of the three variations may be employed.

1. Start with a bounding box prompt: Our results demonstrated that the bounding box method consistently yielded the best performance among the different prompting strategies, even with small variations. Therefore, we recommend that physicians begin the segmentation process by providing a bounding box prompt enclosing the region of interest.
2. Choose the best prediction from the three outputs: SAM generates three segmentation masks in response to an input image and prompt, each representing a different interpretation of the intended region’s size. Physicians should visually inspect and compare the three generated masks against the original image. By identifying the mask that best aligns with the desired region, one can obtain a reliable starting point for further refinement, if necessary.
3. Refine the segmentation using point prompts: In cases where the initial segmentation requires further adjustments, physicians can employ point prompts to guide SAM in including or excluding specific regions from the segmentation. By providing additional prompts on areas that need improvement, physicians can iteratively refine the segmentation output until it accurately represents the target region.

This approach ensures that the model’s output aligns with the physician’s expert knowledge, resulting in accurate and reliable segmentation outcomes for different clinical applications and imaging modalities.

## 5 Conclusion and Future Work

This study assessed the performance of SAM using eight prompting strategies on six datasets from four 2D medical image modalities. We analyzed their advantages and drawbacks in diverse scenarios for the three SAM ViT sizes. SAM exhibited exceptional performance, especially for a zero-shot approach, achieving solid results compared to SOTA segmentation methods tailored or fine-tuned for medical imaging. SAM surpassed the current best performance on the BUSI dataset by a significant margin. Collectively, our findings indicate that SAM holds excellent promise as a medical image segmentation tool.

Based on our findings, we propose a guideline that is practical to implement, requires minimal interaction, and produces solid results in medical imaging segmentation with SAM. By utilizing the bounding box method and refining the segmentation with point prompts, physicians can effectively leverage SAM’s potential to achieve accurate results while retaining control over the process. Additionally, given the comparable performance of the three SAM model sizes, any of them can be employed depending on the available hardware resources.

Segmentations produced with SAM have the potential to surpass even the most stringent quality standards with minimal input from physicians. Our results raise concerns about the quality of some manually annotated ground truth masks, as SAM segmentations appear to delineate the ROI better in some cases. This is particularly noteworthy for labeling new datasets, as it drastically reduces the time and effort required for this monotonous and exhausting task.

As such, SAM-generated segmentations holds immense promise for streamlining data annotation processes and optimizing workflow efficiency in medical image analysis.

Future research could further enhance SAM's capabilities in this domain, achieving even higher performance while retaining SAM's extensive refinement options. Additionally, exploring the potential of adapting SAM for 3D medical imaging is a valuable avenue for investigation, as it would broaden the model's applicability to an even wider range of medical imaging tasks.

## Bibliography

- [1] Shuo Wang, Mu Zhou, Zaiyi Liu, Zhenyu Liu, Dongsheng Gu, Yali Zang, Di Dong, Olivier Gevaert, and Jie Tian. Central focused convolutional neural networks: Developing a data-driven model for lung nodule segmentation. *Medical image analysis*, 40:172–183, 2017.
- [2] Dzung L Pham, Chenyang Xu, and Jerry L Prince. Current methods in medical image segmentation. *Annual review of biomedical engineering*, 2(1):315–337, 2000.
- [3] Olaf Ronneberger, Philipp Fischer, and Thomas Brox. U-net: Convolutional networks for biomedical image segmentation. In *Medical Image Computing and Computer-Assisted Intervention–MICCAI 2015: 18th International Conference, Munich, Germany, October 5–9, 2015, Proceedings, Part III 18*, pages 234–241. Springer, 2015.
- [4] Jie Liu, Yixiao Zhang, Jieneng Chen, Junfei Xiao, Yongyi Lu, Bennett A. Landman, Yixuan Yuan, Alan L. Yuille, Yucheng Tang, and Zongwei Zhou. Clip-driven universal model for organ segmentation and tumor detection. *CoRR*, abs/2301.00785, 2023.
- [5] Litao Yang, Chao Fan, Hao Lin, and Yingying Qiu. Rema-net: An efficient multi-attention convolutional neural network for rapid skin lesion segmentation. *Computers in Biology and Medicine*, page 106952, 2023.
- [6] Geert Litjens, Thijs Kooi, Babak Ehteshami Bejnordi, Arnaud Arindra Adiyoso Setio, Francesco Ciompi, Mohsen Ghahforian, Jeroen Awm Van Der Laak, Bram Van Ginneken, and Clara I Sánchez. A survey on deep learning in medical image analysis. *Medical image analysis*, 42:60–88, 2017.
- [7] Alexey Dosovitskiy, Lucas Beyer, Alexander Kolesnikov, Dirk Weissenborn, Xiaohua Zhai, Thomas Unterthiner, Mostafa Dehghani, Matthias Minderer, Georg Heigold, Sylvain Gelly, et al. An image is worth 16x16 words: Transformers for image recognition at scale. *arXiv preprint arXiv:2010.11929*, 2020.
- [8] Alexander Kirillov, Eric Mintun, Nikhila Ravi, Hanzi Mao, Chloe Rolland, Laura Gustafson, Tete Xiao, Spencer Whitehead, Alexander C Berg, Wan-Yen Lo, et al. Segment anything. *arXiv preprint arXiv:2304.02643*, 2023.
- [9] Chiranji Lal Chowdhary and D Prasanna Acharjya. Segmentation and feature extraction in medical imaging: a systematic review. *Procedia Computer Science*, 167:26–36, 2020.
- [10] Neeraj Sharma and Lalit M Aggarwal. Automated medical image segmentation techniques. *Journal of medical physics*, 35(1):3–14, 2010.
- [11] S Shirly and K Ramesh. Review on 2d and 3d mri image segmentation techniques. *Current Medical Imaging*, 15(2):150–160, 2019.
- [12] Marin Bencevic, Irena Galic, Marija Habijan, and Danilo Babin. Training on polar image transformations improves biomedical image segmentation. *IEEE Access*, 9:133365–133375, 2021.

- [13] Emerald U. Henry, Onyeka Emebob, and Conrad Asotie Omonhinmin. Vision transformers in medical imaging: A review. *CoRR*, abs/2211.10043, 2022.
- [14] Ashish Vaswani, Noam Shazeer, Niki Parmar, Jakob Uszkoreit, Llion Jones, Aidan N Gomez, Lukasz Kaiser, and Illia Polosukhin. Attention is all you need. In I. Guyon, U. Von Luxburg, S. Bengio, H. Wallach, R. Fergus, S. Vishwanathan, and R. Garnett, editors, *Advances in Neural Information Processing Systems*, volume 30. Curran Associates, Inc., 2017.
- [15] Hugo Touvron, Matthieu Cord, Matthijs Douze, Francisco Massa, Alexandre Sablayrolles, and Hervé Jégou. Training data-efficient image transformers & distillation through attention. In *International conference on machine learning*, pages 10347–10357. PMLR, 2021.
- [16] Wenhai Wang, Enze Xie, Xiang Li, Deng-Ping Fan, Kaitao Song, Ding Liang, Tong Lu, Ping Luo, and Ling Shao. Pyramid vision transformer: A versatile backbone for dense prediction without convolutions. In *Proceedings of the IEEE/CVF international conference on computer vision*, pages 568–578, 2021.
- [17] Ziyu Guo, Renrui Zhang, Longtian Qiu, Xianzheng Ma, Xupeng Miao, Xuming He, and Bin Cui. Calip: Zero-shot enhancement of clip with parameter-free attention. *arXiv preprint arXiv:2209.14169*, 2022.
- [18] Hieu Pham, Zihang Dai, Golnaz Ghiasi, Hanxiao Liu, Adams Wei Yu, Minh-Thang Luong, Mingxing Tan, and Quoc V Le. Combined scaling for zero-shot transfer learning. *arXiv preprint arXiv:2111.10050*, 2021.
- [19] Alec Radford, Jong Wook Kim, Chris Hallacy, Aditya Ramesh, Gabriel Goh, Sandhini Agarwal, Girish Sastry, Amanda Askell, Pamela Mishkin, Jack Clark, et al. Learning transferable visual models from natural language supervision. In *International conference on machine learning*, pages 8748–8763. PMLR, 2021.
- [20] Jongseong Jang, Daeun Kyung, Seung Hwan Kim, Honglak Lee, Kyunghoon Bae, and Edward Choi. Significantly improving zero-shot x-ray pathology classification via fine-tuning pre-trained image-text encoders. *arXiv preprint arXiv:2212.07050*, 2022.
- [21] Zifeng Wang, Zhenbang Wu, Dinesh Agarwal, and Jimeng Sun. Medclip: Contrastive learning from unpaired medical images and text. *arXiv preprint arXiv:2210.10163*, 2022.
- [22] Noel C. F. Codella, Veronica Rotemberg, Philipp Tschandl, M. Emre Celebi, Stephen W. Dusza, David A. Gutman, Brian Helba, Aadi Kalloo, Konstantinos Liopyris, Michael A. Marchetti, Harald Kittler, and Allan Halpern. Skin lesion analysis toward melanoma detection 2018: A challenge hosted by the international skin imaging collaboration (ISIC). *CoRR*, abs/1902.03368, 2019.
- [23] Philipp Tschandl, Cliff Rosendahl, and Harald Kittler. The HAM10000 dataset: A large collection of multi-source dermatoscopic images of common pigmented skin lesions. *CoRR*, abs/1803.10417, 2018.
- [24] Philipp Tschandl, Christoph Rinner, Zoe Apalla, Giuseppe Argenziano, Noel Codella, Allan Halpern, Monika Janda, Aimilios Lallas, Caterina

- Longo, Josep Malvehy, John Paoli, Susana Puig, Cliff Rosendahl, H. Peter Soyer, Iris Zalaudek, and Harald Kittler. Human-computer collaboration for skin cancer recognition. *Nature Medicine*, 26(8):1229–1234, June 2020.
- [25] Stefan Jaeger, Alexandros Karargyris, Sema Candemir, Les R. Folio, Jenifer Siegelman, Fiona M. Callaghan, Zhiyun Xue, Kannappan Palaniappan, Rahul K. Singh, Sameer K. Antani, George R. Thoma, Yi-Xiang J. Wang, Pu-Xuan Lu, and Clement J. McDonald. Automatic tuberculosis screening using chest radiographs. *IEEE Trans. Medical Imaging*, 33(2):233–245, 2014.
- [26] Sema Candemir, Stefan Jaeger, Kannappan Palaniappan, Jonathan P. Musco, Rahul K. Singh, Zhiyun Xue, Alexandros Karargyris, Sameer K. Antani, George R. Thoma, and Clement J. McDonald. Lung segmentation in chest radiographs using anatomical atlases with nonrigid registration. *IEEE Trans. Medical Imaging*, 33(2):577–590, 2014.
- [27] Daniel Gut. X-ray images of the hip joints, 2021.
- [28] Jorge Bernal, Francisco Javier Sánchez, Gloria Fernández-Esparrach, Debora Gil, Cristina Rodríguez de Miguel, and Fernando Vilariño. WM-DOVA maps for accurate polyp highlighting in colonoscopy: Validation vs. saliency maps from physicians. *Comput. Medical Imaging Graph.*, 43:99–111, 2015.
- [29] Walid Al-Dhabyani, Mohammed Gomaa, Hussien Khaled, and Aly Fahmy. Dataset of breast ultrasound images. *Data in Brief*, 28:104863, 2020.
- [30] Minki Kim and Byoung-Dai Lee. Automatic lung segmentation on chest x-rays using self-attention deep neural network. *Sensors*, 21(2):369, 2021.
- [31] Tarun Agrawal and Prakash Choudhary. Rese-net: Enhanced unet architecture for lung segmentation in chest radiography images. *Computational Intelligence*.
- [32] Bangcheng Zhan, Enmin Song, and Hong Liu. Fsa-net: Rethinking the attention mechanisms in medical image segmentation from releasing global suppressed information. *Computers in Biology and Medicine*, page 106932, 2023.
- [33] Alessandro Sebastian Podda, Riccardo Balia, Silvio Barra, Salvatore Carta, Gianni Fenu, and Leonardo Piano. Fully-automated deep learning pipeline for segmentation and classification of breast ultrasound images. *Journal of Computational Science*, 63:101816, 2022.

## 6 Supplementary Material

Dataset	Model	Pred	CP	RP	RP3	RP5	BB	BBS5	BBS10	BBS20
ISIC	ViT-H	1st	0.538	0.531	0.762	0.774	0.745	0.737	0.715	0.603
		2nd	0.718	0.677	0.769	0.788	0.845	0.842	0.833	0.789
		3rd	0.375	0.363	0.390	0.483	<b>0.872</b>	0.868	0.860	0.816
	ViT-L	1st	0.704	0.665	0.703	0.700	<b>0.864</b>	0.861	0.852	0.805
		2nd	0.518	0.521	0.768	0.794	0.763	0.757	0.733	0.623
		3rd	0.382	0.366	0.358	0.362	0.841	0.836	0.819	0.730
	ViT-B	1st	0.366	0.355	0.354	0.375	<b>0.870</b>	0.866	0.855	0.810
		2nd	0.665	0.618	0.692	0.695	0.825	0.823	0.807	0.751
		3rd	0.504	0.490	0.766	0.790	0.640	0.631	0.601	0.496
HAM	ViT-H	1st	0.544	0.527	0.752	0.765	0.732	0.724	0.700	0.589
		2nd	0.729	0.686	0.768	0.785	0.838	0.835	0.824	0.778
		3rd	0.420	0.406	0.443	0.541	<b>0.865</b>	0.861	0.851	0.809
	ViT-L	1st	0.731	0.689	0.723	0.721	<b>0.859</b>	0.856	0.846	0.799
		2nd	0.522	0.518	0.764	0.793	0.766	0.761	0.740	0.626
		3rd	0.435	0.413	0.406	0.408	0.830	0.824	0.805	0.699
	ViT-B	1st	0.414	0.403	0.401	0.425	<b>0.863</b>	0.859	0.846	0.799
		2nd	0.659	0.607	0.681	0.683	0.810	0.807	0.795	0.740
		3rd	0.478	0.431	0.749	0.772	0.619	0.610	0.578	0.466
CXR	ViT-H	1st	0.904	0.863	0.923	0.927	0.936	0.934	0.911	0.686
		2nd	0.758	0.727	0.766	0.828	<b>0.942</b>	0.939	0.929	0.826
		3rd	0.471	0.469	0.482	0.514	0.935	0.930	0.913	0.803
	ViT-L	1st	0.834	0.814	0.786	0.776	0.932	0.929	0.916	0.805
		2nd	0.915	0.870	0.930	0.929	0.940	0.936	0.906	0.660
		3rd	0.472	0.471	0.468	0.474	<b>0.945</b>	0.942	0.928	0.758
	ViT-B	1st	0.459	0.459	0.467	0.497	0.916	0.910	0.894	0.817
		2nd	0.804	0.782	0.786	0.803	<b>0.937</b>	0.933	0.921	0.813
		3rd	0.882	0.813	0.928	0.932	0.916	0.898	0.818	0.524
HJXR-F	ViT-H	1st	0.876	0.822	0.941	0.948	0.924	0.908	0.848	0.618
		2nd	0.743	0.767	0.767	0.776	<b>0.962</b>	0.958	0.904	0.746
		3rd	0.517	0.543	0.548	0.599	0.949	0.945	0.905	0.723
	ViT-L	1st	0.773	0.800	0.788	0.791	<b>0.972</b>	0.969	0.951	0.843
		2nd	0.874	0.804	0.927	0.944	0.925	0.922	0.844	0.685
		3rd	0.516	0.540	0.540	0.619	0.961	0.944	0.818	0.448
	ViT-B	1st	0.466	0.486	0.481	0.489	0.924	0.915	0.888	0.788
		2nd	0.733	0.775	0.742	0.727	<b>0.958</b>	0.954	0.926	0.771
		3rd	0.911	0.774	0.909	0.907	0.899	0.876	0.735	0.490



Dataset	Model	Pred	CP	RP	RP3	RP5	BB	BBS5	BBS10	BBS20
HJXR-I	ViT-H	1st	0.211	0.742	0.808	0.828	<b>0.875</b>	0.866	0.734	0.624
		2nd	0.393	0.479	0.449	0.491	0.855	0.849	0.790	0.620
		3rd	0.294	0.295	0.316	0.384	0.800	0.796	0.758	0.629
	ViT-L	1st	0.363	0.540	0.448	0.451	0.824	0.817	0.748	0.594
		2nd	0.165	0.758	0.864	0.860	<b>0.887</b>	0.877	0.762	0.555
		3rd	0.301	0.306	0.292	0.330	0.862	0.841	0.733	0.580
	ViT-B	1st	0.259	0.303	0.328	0.368	0.772	0.767	0.734	0.591
		2nd	0.403	0.502	0.467	0.478	<b>0.849</b>	0.843	0.802	0.615
		3rd	0.314	0.717	0.823	0.830	0.838	0.838	0.779	0.622
CVC	ViT-H	1st	0.716	0.763	0.861	0.880	0.889	0.881	0.835	0.702
		2nd	0.554	0.544	0.642	0.754	<b>0.926</b>	0.924	0.916	0.844
		3rd	0.232	0.224	0.224	0.245	0.924	0.922	0.918	0.868
	ViT-L	1st	0.498	0.482	0.508	0.522	<b>0.920</b>	0.918	0.906	0.853
		2nd	0.702	0.728	0.836	0.841	0.873	0.867	0.818	0.672
		3rd	0.229	0.222	0.217	0.223	0.909	0.904	0.870	0.773
	ViT-B	1st	0.234	0.225	0.222	0.226	<b>0.920</b>	0.916	0.906	0.833
		2nd	0.447	0.440	0.495	0.510	0.907	0.906	0.892	0.796
		3rd	0.644	0.688	0.778	0.783	0.821	0.810	0.758	0.585
BUSI	ViT-H	1st	0.583	0.541	0.736	0.766	0.754	0.744	0.713	0.631
		2nd	0.641	0.616	0.688	0.735	0.840	0.837	0.823	0.768
		3rd	0.192	0.184	0.196	0.254	<b>0.863</b>	0.859	0.848	0.800
	ViT-L	1st	0.656	0.649	0.674	0.663	<b>0.866</b>	0.862	0.855	0.794
		2nd	0.567	0.536	0.748	0.779	0.782	0.777	0.754	0.649
		3rd	0.228	0.205	0.202	0.252	0.849	0.847	0.830	0.741
	ViT-B	1st	0.202	0.192	0.181	0.213	<b>0.884</b>	0.881	0.869	0.823
		2nd	0.634	0.604	0.682	0.691	0.832	0.830	0.818	0.766
		3rd	0.562	0.522	0.773	0.797	0.725	0.722	0.689	0.582

Table 5: DSC of predictions for six datasets using the eight proposed prompt strategies for the three SAM ViT sizes.